Materials Today Nano 23 (2023) 100377

Contents lists available at ScienceDirect

Materials Today Nano

journal homepage: www.sciencedirect.com/journal/materials-today-nano

Periodic anti-phase boundaries and crystal superstructures in $PtCu_3$ nanoparticles as fuel cell electrocatalysts

A.R. Kamšek [a, b], A. Meden [b], I. Arčon [c, d], P. Jovanovič [a], M. Šala [e], F. Ruiz-Zepeda [a], G. Dražić [a], M. Gaberšček [a], M. Bele [a, **], N. Hodnik [a, *]

[a] Department of Materials Chemistry, National Institute of Chemistry, Hajdrihova 19, 1000 Ljubljana, Slovenia
[b] Faculty of Chemistry and Chemical Technology, University of Ljubljana, Večna pot 113, Ljubljana 1000, Slovenia
[c] Laboratory of Quantum Optics, University of Nova Gorica, Vipavska 13, 5000 Nova Gorica, Slovenia
[d] Department of Low and Medium Energy Physics, Jožef Stefan Institute, Jamova 39, 1000 Ljubljana, Slovenia
[e] Department of Analytical Chemistry, National Institute of Chemistry, Hajdrihova 19, 1000 Ljubljana, Slovenia

ARTICLE INFO

Article history:
Received 12 April 2023
Received in revised form
16 June 2023
Accepted 7 July 2023
Available online 17 July 2023

Keywords:
Nanoparticles
Defects
anti-phase boundary
Superstructures
Electrochemistry
Electrocatalysis

ABSTRACT

To reduce the cost of the electrocatalyst for the oxygen reduction reaction in proton exchange membrane fuel cells, supported metal alloy nanoparticles are commonly used to decrease the amount of the scarce and expensive Pt. Since the structure of the nanoparticles has a crucial influence on the catalytic properties, advanced characterization methods help elucidate these relationships and ultimately enable more rational synthesis. This work focuses on investigating the presence of one particular planar defect, namely periodic anti-phase boundaries in carbon-supported $PtCu_3$ nanoparticles. The studying of this structural phenomenon was approached with several characterization tools. *Ex-situ* X-ray diffractograms were used in conjunction with computer simulations and Rietveld analyses to reliably determine the modulated unit cell containing anti-phase boundaries, while their temperature-dependent formation and disappearance were observed with high-temperature X-ray powder diffraction. In addition, their presence was also confirmed by electron diffraction and atomically resolved scanning transmission electron microscopy. Furthermore, the average neighborhood of Cu and Pt atoms was confirmed using extended X-ray absorption fine structure. Finally, the electrocatalytic activity for the oxygen reduction reaction for composites with and without anti-phase boundaries was determined using a thin-film rotating disk electrode, and the performance was found to correlate with the degree of alloy ordering but not with the presence of anti-phase boundaries. Overall, this study represents a significant step towards better control over the atomically precise synthesis of advanced functional metallic materials by providing valuable insight into the formation of planar defects in metallic alloy nanoparticles and their impact on the structure-property relationships of electrocatalysts.

1. Introduction

With the pressing climate issues due to our excessive resource consumption, there is a great need to shift to a new energy landscape relying on clean and sustainable energy conversion and storage. Among the proposed solutions, hydrogen technologies stand a realistic chance of achieving a market breakthrough in both transport and stationary power generation. To improve the cost-effectiveness of electrocatalysts in proton exchange membrane fuel cells, commonly containing scarce and expensive metals, synthesizing metallic nanoparticles and alloying them with more abundant transition metals is a common strategy [1]. Carbon-supported platinum-copper nanoparticles are a well-known catalyst, used for the oxygen reduction reaction (ORR). Such ensembles of nanoparticles can exhibit a variety of structural differences, including sizes, morphologies, compositions, crystal structures, internal strains, and a diverse range of defects, all of which govern their catalytic properties *via* the well-known concept of structure-function relationship [2–6]. Despite many efforts, a comprehensive prediction of the catalytic properties based on atomic-level structural features remains a complex challenge [7–10].

* Corresponding author.
** Corresponding author.
E-mail addresses: marjan.bele@ki.si (M. Bele), nejc.hodnik@ki.si (N. Hodnik).

https://doi.org/10.1016/j.mtnano.2023.100377

Generally, nanoparticulate Pt-M (M = Cu, Co, Ni, Fe) systems are well studied from the structural point of view. The dynamics and particle growth mechanisms during a Pt—Cu order-disorder transition were revealed in an *in-situ* heating transmission electron microscopy (TEM) study [11] and in a high-temperature X-ray diffraction (HT-XRD) study [12]. Additionally, *in-situ* TEM was used to monitor the ordering in Pt—Fe nanoalloys [13] while HT-XRD was used to track ordering in Pt—Fe, Pt—Co, and Pt—Ni nanoalloys [14]. For a Pt_3Co system, a study correlated the degree of order to catalyst durability using both *in-situ* XRD and TEM [15]. Ultimately, copper dissolution was tracked to show the beneficial effect of alloy ordering on ORR activity and electrochemical stability for Pt—Cu nanoparticles [16]. The promising potential of intermetallic alloys was also demonstrated for other Pt-based systems [17]. These studies, however, did not consider all possible crystallographic structures and/or defects and their potential impact on electrocatalysis.

This is especially relevant for Cu—Pt alloys with a composition close to Cu_3Pt, where another phase appears at the transition from the ordered phase to the disordered one, namely a long-period structure derived from the ordered phase featuring periodic anti-phase boundaries (APBs). APBs are planar defects, separating domains of the ordered Pm-3m phase by translating the Pm-3m structure by half of its unit cell along one of the sides of the cubic cell [18]. The size of the so-formed superstructure unit cell, dependent on chemical composition and annealing temperature, was previously determined with single-crystal X-ray diffraction [18,19]. The ordering process and APB presence were studied by electron diffraction and dark field microscopy to elucidate domain growing for a bulk alloy [20] and by *in-situ* TEM to confirm the continuous behavior of the transition [21]. This two-step order-disorder transition was also confirmed by measuring specific heat [18] and magnetic susceptibility [22]. Analogous long-period structures were reported for Cu_3Au and Cu_3Pd bulk alloys [23—26].

While there are several studies of long-period structures in bulk Cu—Pt alloys, the same cannot be said for nanoparticulate systems. APBs receive considerable attention in the magnetic nanomaterials community, as the differences in magnetic properties among different materials are in part attributed to such changes in the local structure [27—30]. Studies of this intriguing phase transition are challenging due to difficulties with *in-situ* techniques that are capable of tracking structural changes under necessary conditions in real time. To the best of our knowledge, APBs have not yet been studied in supported Cu_3Pt nanoparticles as an ORR electrocatalyst.

The ability to engineer such defects determines the significance of the present work for the electrocatalysis community, especially when attempting to increase the number of active sites in electrocatalysts and thus locally tune their catalytic behavior through structural changes [31]. Besides anti-phase boundaries, also stacking faults, grain boundaries, and other structural features can be present in nanoparticulate systems. In the field of oxygen reduction catalysis, several materials with enhanced activity containing twin and other grain boundaries were found [32—39]. Among those, several studies also report enhanced electrochemical stability [33,35,37] along with successful application to methanol oxidation reaction [34,36]. On the other hand, a detrimental effect of the grain boundaries on ORR activity was demonstrated for PtCo nanowires [40]. This confirms that since the presence of planar defects can tune the catalytic behavior, a more thorough understanding is needed to reach a consensus on how various defects influence the structure-property relationship.

Outside of ORR electrocatalysis, multiple studies are confirming the impact of planar defects on the catalytic properties. Various grain-boundary-rich nanostructures exhibited an improved activity for hydrogen oxidation [41], ethanol oxidation [42,43], methanol oxidation [43], CO_2 reduction [44], and CO reduction [45]. More specifically, systems containing stacking faults were successful in improving the activity for hydrogen evolution [46,47], methanol oxidation [48], methane oxidation [49], and oxidation of formic acid [48,50]. A number of those studies also reported enhanced electrochemical stability [42,43,46—48]. Such studies are a good motivation to continue in the direction of defect-oriented research also in ORR electrocatalysis, complementing existing studies on alloy ordering and core-shell nanoparticle morphologies [2,51].

This work encompasses a comprehensive structural analysis of carbon-supported $PtCu_3$ nanoparticles exhibiting long-period structures containing anti-phase boundaries. Accordingly, we employed two different synthesis strategies to induce the formation of APBs in nanoparticles. We used both *ex-situ* and *in-situ* XRD to characterize their crystal structure and probed the local neighborhood with extended X-ray absorption fine structure (EXAFS) while scanning transmission electron microscopy (STEM) was employed to obtain information in real space. Experimental results were supported with simulations of APB manifestation under XRD and STEM. Finally, we performed thin-film rotating disk electrode (TF-RDE) measurements to evaluate the performance of electrocatalysts towards ORR. This study provides valuable results and insights into the formation of superstructures in nanoparticulate electrocatalysts. Specifically, it presents new knowledge on anti-phase boundaries in $PtCu_3$ nanoparticles, including in the context of their catalytic activity. This work paves the way for a fully controlled and smart design of advanced functional materials.

2. Methods

2.1. Synthesis

Samples were synthesized according to two different synthesis strategies, namely the two-step and the one-step approach. The two-step synthesis of Cu_3Pt/C samples was extensively reported elsewhere [51—53]. Briefly, a Cu/C precursor was suspended in water, and 0.1 M K_2PtCl_4 was added in two steps. The resulting composite was annealed at 310 °C for 1 h in air, then at 750 °C in a H_2(5%)/Ar atmosphere for 15 min and cooled down with a rate of 3 °C/min to room temperature (RT) to yield the first set of samples. Initial annealing in the presence of oxygen was previously shown to prevent the growth of unwanted carbon deposits on the nanoparticle surface [54]. Subsequent annealing at a high temperature enabled mixing of platinum and copper in a solid solution, while partial alloy ordering was achieved with slow cooling. Annealing in the presence of H_2 was employed to prevent any oxidation from taking place.

In the one-step synthesis, we used a modified sol-gel procedure to increase the homogeneity of Cu_3Pt/C. First, 0.8 g of hydroxyethylcellulose (Merck, Germany) was dissolved in 6 mL of water at 90 °C. Then, 0.18 g of copper(II)acetate monohydrate (Honeywell, Germany) and 0.12 g of tetraamine platinum(II)nitrate (Sigma-Aldrich, Germany) was dissolved in a viscous solution at 50 °C by mixing. Carbon black (Vulcan XC72R, Cabot, USA) was added to the solution, and the resulting mixture was frozen with liquid nitrogen and vacuum dried. In the next step, the dried mixture was heated to 250 °C in an air atmosphere at a heating rate of 2 °C/min and then left at this temperature for 2 h. After 1 h, when the desired temperature was reached, the atmosphere was changed. The sample was ventilated with argon (gas flow rate 100 mL/min) for 15 min and then with a mixture of H_2(5%)/Ar until the heat treatment was completed. After 2 h at 250 °C, the composite material was heated at a rate of 2 °C/min to 850 °C for 6 h, then cooled to RT at a rate of 6 °C/min and aerated with argon (gas flow rate 100 mL/min) for 15 min. Then, the sample was heat-treated again in an air

atmosphere by heating it to 310 °C at a heating rate of 5 °C/min and left at this temperature for 2 h. After 1 h, when the desired temperature was reached, the atmosphere was changed. The sample was aerated with argon (gas flow rate 100 mL/min) for 15 min and then with a mixture of H_2/Ar until the completion of heat treatment to yield the first set of samples.

For both syntheses, the resulting composites were then annealed according to different protocols to promote the formation of various crystal phases. The second set was obtained by heating the first one at a rate of 2 °C/min to 575 °C in H_2/Ar, annealing it at that temperature for 48 h, and rapidly cooling it down to RT. For the one-step synthesis, two more samples were generated. The third sample was obtained by heating the second one at a rate of 5 °C/min to 750 °C in a H_2/Ar atmosphere, annealing it for 30 min, and rapidly cooling it down to RT. The fourth sample was obtained by similarly annealing the second one at 750 °C in a H_2/Ar atmosphere for 1 h, cooling it down at a rate of 6 °C/min to 575 °C for 24 h, and rapidly cooling it down to RT. Rapid cooling was performed to preserve the crystal phases, present at higher temperatures.

2.2. X-ray diffraction

X-ray diffractograms were recorded on a PANalytical X'Pert PRO MPD diffractometer with Cu Kα_1 radiation in the 2θ range from 5° to 140° using a step size of 0.008° and a holding time of 450 s. Samples were prepared on a Si holder.

High-temperature XRD was performed using a PANalytical X'Pert PRO HTK diffractometer with Cu Kα radiation from 20° to 60° using a step size of 0.053° and a holding time of 450 s. Scans were recorded at RT and higher temperatures according to a temperature-time profile chosen for each experiment. Samples were prepared on a corundum holder.

2.3. XRD profile analysis

Simulations of different superstructure phases were carried out with GSAS-II software [55]. Rietveld analysis was performed using TOPAS-Academic (Version 7) [56] to determine the weight fractions and unit cell parameters of crystal phases. The following fit parameters were used: background coefficients, phase fractions, unit cell parameters, and anisotropic peak broadening. The latter was used due to the observed varying peak widths in different directions. The quality of the refinement was evaluated with the R-weighted pattern (R_{wp}) value. The stoichiometric composition of each phase was determined using Vegard's rule on the calculated lattice parameters.

2.4. DIFFaX simulations of XRD patterns

DIFFaX software was used to simulate XRD patterns of structures featuring twin defects [57]. For the Cu_3Pt Pm-3m phase, diffraction patterns of structures with and without twin boundaries were calculated, with twin boundaries being parallel to {111} planes. Structures were written with an alternative unit cell, where one of the axes was parallel to the {111} plane normal. Structures with 0%, 2%, 5% and 10% randomly occurring twin boundaries were considered.

2.5. Electron microscopy

Scanning electron microscopy (SEM) was performed on an ULTRA plus (Carl Zeiss) microscope at 5 kV using an InLens detector. Standard SEM pin mounts (Agar Scientific) covered with conductive carbon tape (Agar Scientific) were used to hold the powder samples.

STEM images were recorded in a probe Cs-corrected scanning transmission electron microscope Jeol ARM 200 CF. The operational voltage was set to 80 kV. The beam convergence semi-angle was 24 mrad. Bright-field and high-angle annular dark-field (HAADF) imaging were performed with 0−45 and 68−185 mrad collection semi-angles, respectively. Selected-area electron diffraction was employed to examine the structure of the materials. Samples were prepared as powders and deposited on a nickel lacy-carbon-coated grid.

2.6. QSTEM simulations of STEM images

Simulations of HAADF STEM images were performed using quantitative image simulation software QSTEM [58] using the multislice method and frozen phonon approximation as well as thermal diffuse scattering with 10 iterations. Models were created using the Pm-3m cubic structure with and without present antiphase boundaries. Instrumental parameters were set to experimentally used values. Poisson noise was added to the obtained images.

2.7. Extended X-ray absorption fine structure

EXAFS spectra of samples after a two-step synthesis were measured at the XAFS beamline of the ELETTRA synchrotron radiation facility in Trieste, Italy. The measured signal was compared with model signals to yield the type and the average number of neighbors, shell radii, and the Debye-Waller factor for the nearest neighbors of Cu and Pt. For a more detailed description of the method, see the Supporting Information.

2.8. Electrochemical characterization via thin-film rotating disk electrode

TF-RDE measurements were conducted at RT in a two-compartment cell in an 0.1 M $HClO_4$ (Merck, Suprapur, 70%) electrolyte with a three-electrode system controlled by a potentiostat (CompactStat, Ivium technologies). A reversible hydrogen electrode (RHE, HydroFlex, Gaskatel) was used as a reference, and a graphite rod was used as a counter electrode. The working electrode was a glassy carbon disc with a geometric surface area of 0.196 cm^2, embedded in Teflon (Pine Instruments). 20 µl of 1 mg/mL water-based catalyst suspension was dropcasted on the electrode. 5 µL of Nafion solution (ElectroChem) diluted in isopropanol (1:50) was deposited on the dry catalyst film.

Initially, the catalyst was activated for 200 cycles between 0.05 and 1.2 V vs. RHE with a scan rate of 300 mVs^{-1} under a rotation rate of 600 rpm in an N_2-saturated electrolyte. Then, the electrolyte was exchanged for a fresh one. ORR polarization curves were measured between 0.05 and 1.0 V vs. RHE with a scan rate of 20 mV^{-1} at 1600 rpm in an O_2-saturated electrolyte. The ohmic resistance of the electrolyte was determined and accounted for as reported previously [59]. ORR kinetic parameters were calculated at 0.9 and 0.95 V vs. RHE. The electrolyte was then purged with CO and saturated with N_2. CO stripping was performed in the same manner as ORR measurements, but without rotation and in an N_2 saturated electrolyte. Electrochemical surface area (ECSA) was determined by integrating the charge in the CO stripping as reported previously [60].

2.9. Elemental analysis with inductively coupled plasma optical emission spectrometry (ICP-OES)

A Varian 715-ES ICP optical emission spectrometer was used to perform elemental analysis. For sample dilution and preparation of

standards, ultrapure water (Milli-Q, Millipore) and ultrapure acids (HNO_3 and HCl, Merck-Suprapur) were used. Standards were prepared in-house by dilution of certified, traceable, ICP-grade single-element standards (Merck CertiPUR). Before ICP-OES analysis, each sample was weighed and digested using a microwave-assisted digestion system (CEM MDS-2000) in a solution of 6 mL HCl and 2 mL HNO_3. The digested samples were cooled to RT and diluted with 2%v/v HNO_3 until their concentration was within the desired concentration range.

3. Results and discussion

Several Pt—Cu analogs were synthesized with two different synthesis strategies and several different annealing protocols. To identify the crystal phases, present in the samples, XRD analysis was performed. As an example, Fig. 1a shows a recorded diffraction pattern for a Cu_3Pt/C sample after a one-step synthesis that underwent thermal annealing at 575 °C in a reductive atmosphere (the second set, as described in 2.1). In nanoparticulate systems, it is possible that only partial ordering is achieved during annealing even if the phase diagram for bulk systems would predict a single phase at equilibrium [15]. The prominent (111) and (200) diffraction maxima at 42.3°, 49.1° and others confirm the presence of an Fm-3m cubic disordered alloy phase, while other diffraction maxima, such as the (100) reflection at 24.1°, confirm Pm-3m crystal ordering. The satellite peaks near certain Pm-3m reflections, such as around the (110) reflection at 34.2°, reveal the presence of a superstructure. Due to the low intensity of superstructure peaks, longer XRD scans were crucial in obtaining more accurate information about this phase. The superstructure was observed in all samples, where the last annealing step used a temperature of 575 °C.

To determine the exact placement of APBs, several different superstructures were systematically screened by simulating their XRD patterns to yield the probable number of cubic cells on each side of a boundary. Two parameters were varied, namely the overall pseudo-cubic unit cell size and the number of cubic cells on either side of an APB. Fig. 2a shows their effect on the simulated diffraction pattern in the 2θ range where a set of clearly experimentally observable satellite peaks is located, for several different unit cells as depicted in Fig. 2b. For simplicity, only the superstructure phase was used for XRD simulations. From the simulated diffraction patterns, it is apparent that the pseudo-cubic cell size determines the 2θ difference between the simulated peaks with larger cells having satellite peaks closer together, while the placement of the APB determines how prominent multiple satellite peaks are with APBs close to the middle of the cell causing fewer prominent satellite peaks. The best agreement with the experimental observation was achieved for a unit cell consisting of 15 cubic cells with one anti-phase boundary placed right on the cell edge and another one between the 6th and 7th cubic cell as depicted in Fig. 1b. The presence of the recognized crystal phases agrees with past experimental observations of the order-disorder transition for Cu—Pt alloys with a similar stoichiometric ratio with one study reporting a half-period, referring to the number of cubic cells between two APBs, as 6.3 ± 0.1 for a bulk alloy with 25.9 at.% Pt, annealed at 540 °C [18].

The presence of a mixture of different phases makes the Rietveld analysis of diffraction patterns somewhat ambiguous. Long-period structures with a range of different half periods were considered to narrow down the search to structures comprised of 14 or 15 ordered cubic alloy unit cells. Although one superstructure eventually gave the best result, it was not a significantly better fit compared to the second-best performer. Additionally, using a single type of superstructure did not yield a perfect fit, indicating that there may be more than one superstructure present in the sample. Nonetheless, we refrained from attempting to include multiple modulated phases in the Rietveld analysis, because a higher number of fit parameters would likely make the fit less stable, which would introduce further uncertainty to the result.

To quantify the share of each crystal phase, a Rietveld analysis was conducted. Fig. 1a shows the resulting fit along with the difference between the experimental and simulated diffraction patterns. Table 1 summarizes the space groups, their weight fractions, lattice parameters, and calculated ratios between Pt and Cu according to Vegard's rule. The Rietveld analysis confirmed that all three listed phases are present in the sample with the Fm-3m and the superstructure phase being richer in Pt as apparent from the

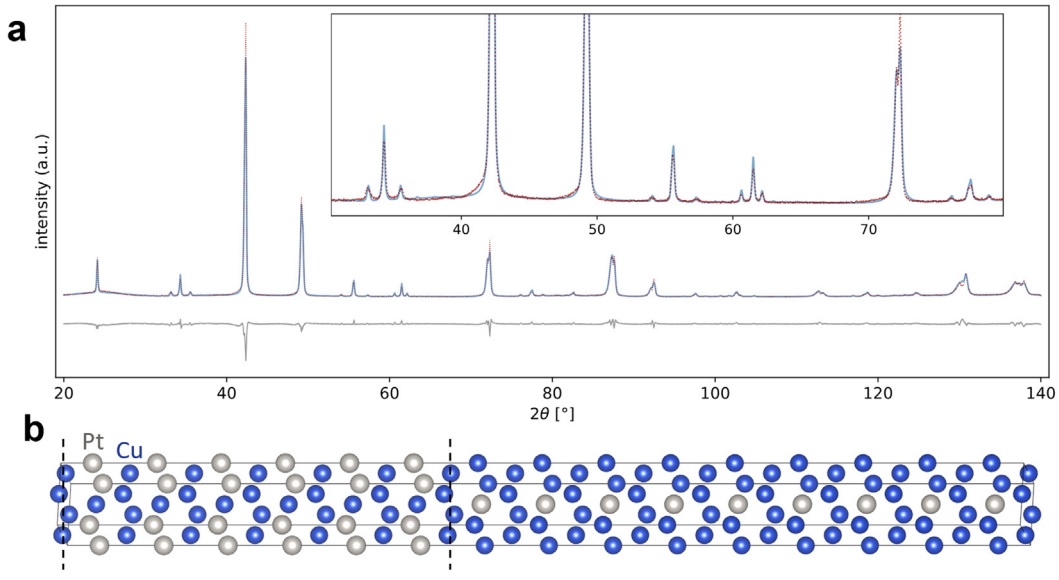

Fig. 1. XRD investigation of a $PtCu_3$/C electrocatalyst annealed at 575 °C. **(a)** XRD pattern with experimentally measured values in dotted red and the Rietveld fit in blue. Below the experimental and simulated diffraction patterns, the difference between them is depicted in grey. Inset shows an enlarged region containing multiple sets of satellite peaks. **(b)** The pseudo-cubic unit cell, used in subsequent diffraction pattern analysis. Black dashed lines denote APBs.

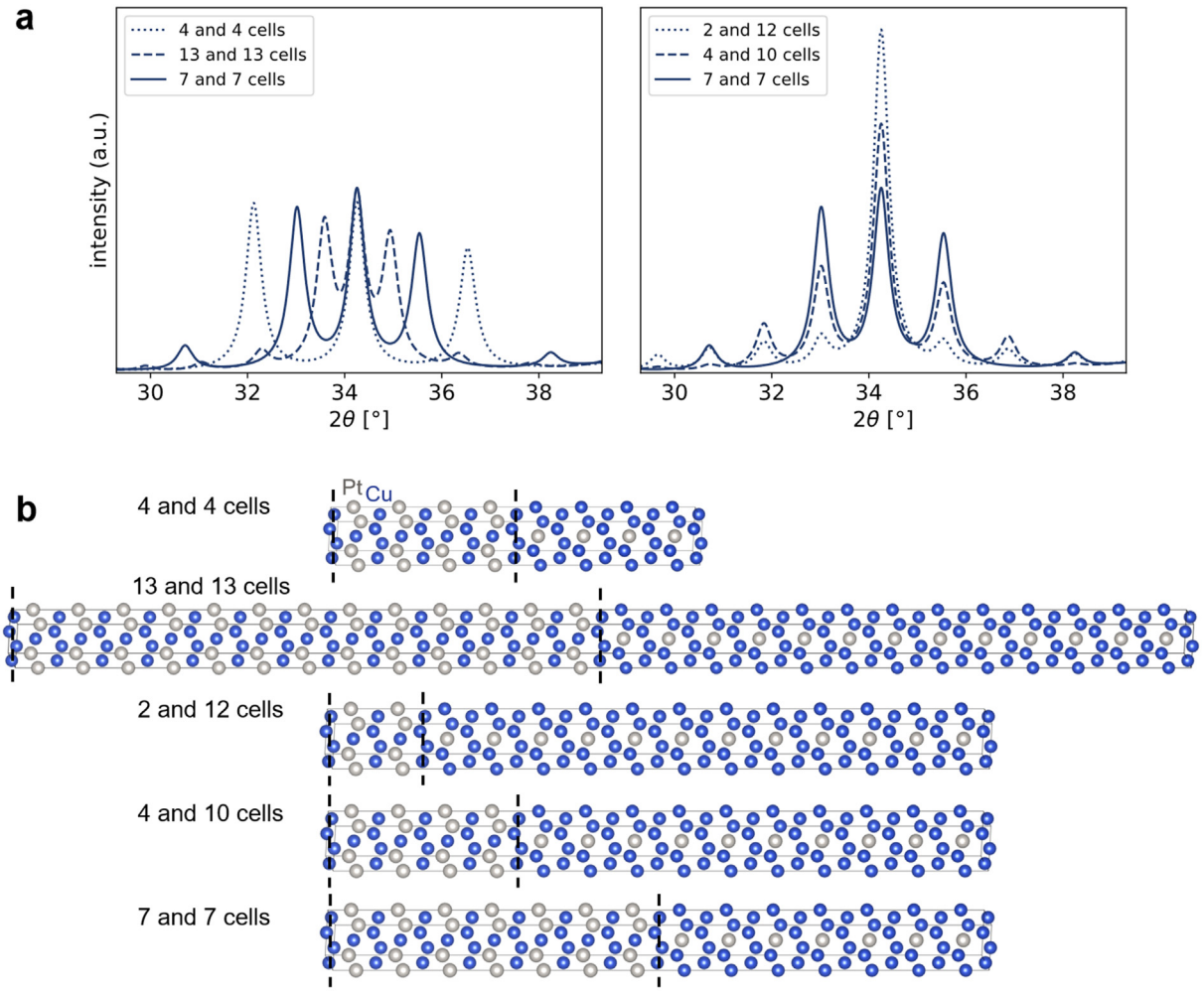

Fig. 2. Determining the placement of APBs in a Pt–Cu pseudo-cubic unit cell. **(a)** Simulated XRD patterns for different choices of modulated cells. **(b)** Unit cells, used in the plotted simulation results. Black dashed lines denote APBs.

Table 1
Rietveld profile fitting results. The last digit uncertainty is given in parentheses following each value. The Rwp value for the fit is 10.0%.

Space group	Unit cell parameters in Å	Weight fraction	Calculated Pt:Cu ratio
Fm-3m	3.702(2)	0.58(1)	1:2.6(1)
Pm-3m	3.692(2)	0.17(1)	1:3.0(1)
P4mm (Pm-3m with APBs)	3.700(2), 55.289(5)	0.25(1)	1:2.6(1)

larger unit cell parameter. In Table 1, two unit cell parameters are listed for the superstructure phase, namely the unit cell parameter for the cubic cells comprising the modulated cell, and the overall cell length. The latter is shorter than the value obtained by multiplying the first parameter by the number of cubic cells, which means the modulated cell's constituent cells are exhibiting slight tetragonality. Different samples yielded similar results in terms of unit cell parameters, as reported in Tables S1 and S2.

To observe the evolution of the crystal phases under controlled temperature, we performed *in-situ* HT-XRD on a sample that did not yet undergo annealing at 575 °C (the first set of samples, as described in Sect. 2.1). As depicted in Fig. 3a, scans were taken first at RT, then at different temperatures between 500 °C and 650 °C, and again at RT. After each temperature change, there was a 5-min pause before the start of recording to allow the entire sample to achieve a uniform temperature. Fig. 3b shows a heatmap of the recorded diffraction patterns with each line corresponding to one diffraction pattern, and white arrows signifying the onset of the long-period structure. Due to a significantly lower signal-to-noise ratio compared to overnight scans at RT, phase identification was the only information obtained from the recordings. To visualize the patterns in a heatmap, the background was subtracted and the square root of intensity was plotted to enhance the visibility of weaker diffraction maxima. The Pm-3m phase becomes prominent around 530 °C, whereas the long-period superstructure presents itself more clearly at 550 °C and disappears at approx. 590 °C. These results indicate that phase transitions are slow and that there is a temperature range where APBs persist, agreeing with literature reports [18,61]. Within that temperature range, the results indicate that the satellite peaks are getting closer together with rising temperature, which signifies a larger size of the modulated unit cell according to the simulations in Fig. 2a. This confirms that APBs are

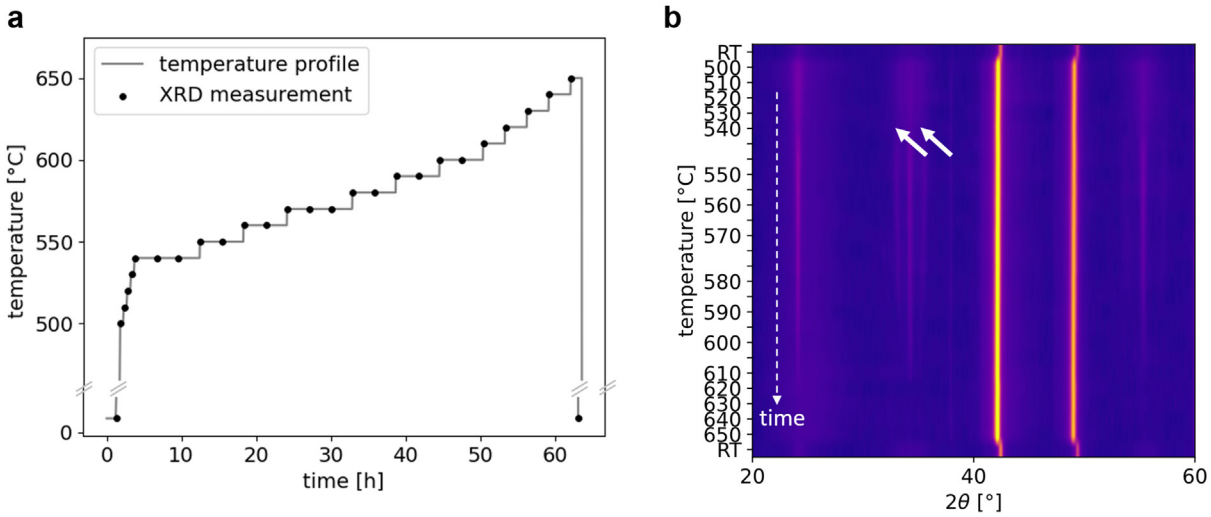

Fig. 3. *In-situ* HT-XRD investigation of a $PtCu_3$/C sample. **(a)** The temperature-time profile used for HT-XRD. Black dots indicate measurements and the grey line indicates the profile. **(b)** A heatmap showing diffraction patterns of a $PtCu_3$/C sample following the temperature-time profile. Colors correspond to square roots of intensity. White arrows signify the onset of the long-period structure.

indeed thermodynamically stable and not a kinetically controlled artifact formation.

Thermal equilibrium states were previously confirmed for this type of structure in bulk [20]. A computer simulation study of the kinetics of the boundary annihilation process was carried out for parallel boundaries in a Cu_3Pt system and found that the superstructure phase with flat boundaries is not only thermally stable but can also remain metastable in the temperature range where the ordered cubic alloy phase is thermally stable [62]. In our HT-XRD experiments, it was confirmed that the formation and annihilation processes were slow and that the long-period superstructure in nanoparticles is stable across a temperature range which is quite consistent with the temperature range reported in a study investigating a bulk alloy [18].

EXAFS analysis was used to analyze the composition of the first coordination shell around Cu and Pt atoms in supported Cu_3Pt nanoparticles after a two-step synthesis before and after prolonged annealing at 575 °C. The average number of Cu and Pt neighbors, their distance from the central (Cu or Pt) atom, and the Debye-Waller factor, which describes a thermal and static disorder in the nearest neighbor coordination shell, were resolved from the collected spectra. Simultaneously, the XRD diffraction patterns of those samples were analyzed with Rietveld analysis to yield the weight fractions of the present crystal phases. The numbers of nearest neighbors according to EXAFS and XRD were found to be within the margin of error, as summarized in Table 2. Considering the uncertainties, arising from both Rietveld analysis and EXAFS analysis, the samples did not differ significantly in their numbers of neighbors in the first coordination shell. Additionally, the determined shell radii showed no obvious local deformations in any of the samples, confirming that all phases were cubic with a comparable unit cell parameter (extended results are given in Table S3 and visualized in Fig. S1).

To complement information about the bulk material, provided by XRD, we turned to electron microscopy to obtain more local data. Fig. 4 depicts STEM images of a sample with Cu_3Pt nanoparticles exhibiting APBs (not seen at this magnification). A significant size polydispersity is present among the nanoparticles with sizes ranging from a few nanometers to a few tens of nanometers. For the most part, nanoparticles are approximately spherical in shape. Figs. S2 and S3 include SEM images confirming the size polydispersity and occasional faceting as well as showing the morphology of the carbon support. In addition, twin boundaries are regularly observed on STEM images of larger nanoparticles, revealed by a contrast change along an entire particle perimeter, especially visible in bright-field imaging. Most commonly, parallel twin boundaries were observed, which most likely formed during thermal annealing through the sintering of multiple crystallites. The increasing amount of parallel twin boundaries in the structure broadens the peaks in diffraction patterns (as summarized in Fig. S4).

Selected-area electron diffraction was used to confirm the presence of a superstructure on a local level. Fig. 5 shows an electron diffraction pattern with visible individual spots, corresponding to Cu_3Pt crystal phases, as well as diffuse rings, corresponding to partially amorphous carbon support. Starting at lower distances in the reciprocal space, the strongest observed ring consisted of overlapping signal from the partially graphitic support and (100) diffraction maxima for the Pm-3m Cu_3Pt phase, followed by (110) Pm-3m maxima and (111) maxima of both Fm-3m and Pm-3m

Table 2
The number of nearest neighbors, as calculated from EXAFS and XRD, for samples after a two-step synthesis. The last digit uncertainty is given in parentheses following each value.

Sample	Neighbors of Pt	N (EXAFS)	N (XRD)	Neighbors of Cu	N (EXAFS)	N (XRD)
Before annealing	Cu	10.2(6)	9.4(4)	Cu	8.4(3)	8.3(4)
	Pt	1.8(6)	2.6(4)	Pt	3.6(3)	3.7(4)
After annealing	Cu	9.8(6)	9.3(4)	Cu	8.6(3)	8.3(4)
	Pt	2.2(6)	2.7(4)	Pt	3.4(3)	3.8(4)

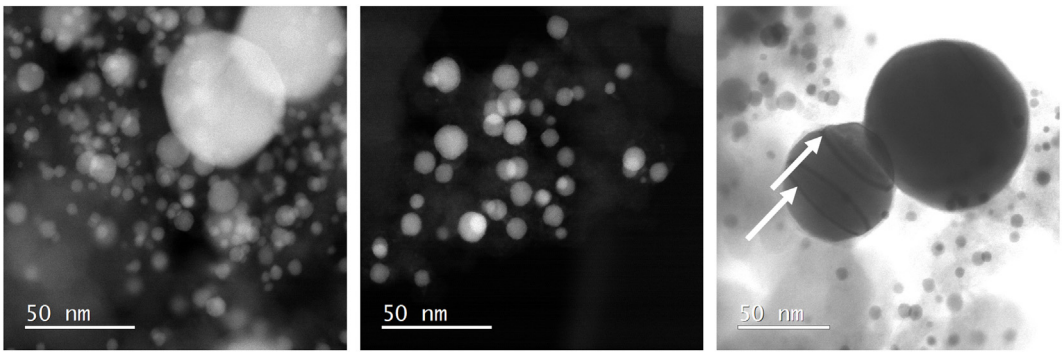

Fig. 4. STEM images of a Cu_3Pt/C sample exhibiting APBs at a lower magnification. Arrows are used to denote the location of parallel twin boundaries in a larger nanoparticle.

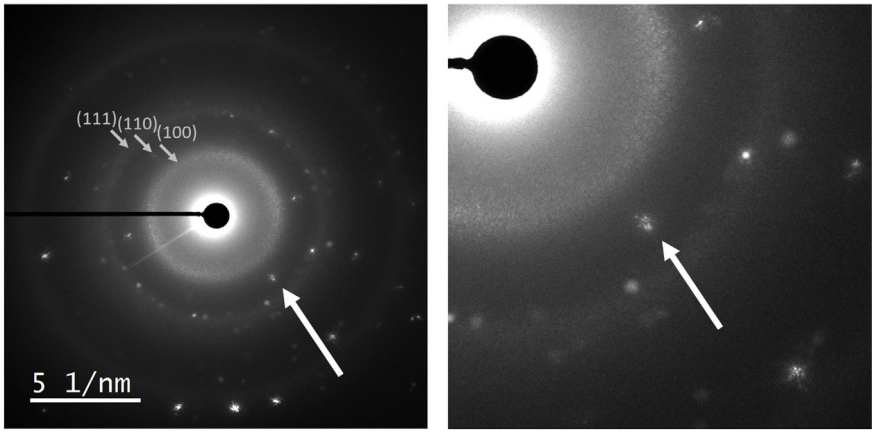

Fig. 5. Selected-area electron diffraction pattern of a Cu_3Pt/C sample exhibiting APBs and an enlarged region thereof. Arrows denote characteristic spot splitting.

phases. The splitting of (110) spots is clearly observed in the diffraction pattern, which is in complete agreement with the satellite peaks, observed with XRD.

Observing APBs at atomic resolution in real space, however, is more elusive because a structure containing APBs is not always distinguishable from the defect-free Pm-3m phase since some of their two-dimensional projections match. Fig. 6 contains results of STEM image simulations of nanoparticles made out of Pm-3m unit cells with and without APBs in different orientations to show their ambiguity in the real-space visualization. The APB manifests itself most clearly in one of the [100] zone axes with the locations of the Pt and Cu atomic columns shifting for half a cubic unit cell, while another [100] projection matches the APB-free one. The APBs manifest themselves less clearly in the commonly used [110] zone axis despite the otherwise noticeable difference in intensity between the Cu and Pt−Cu atomic columns in HAADF imaging. Again, the image in one of the [110] zone axes may match the APB-free Pm-3m one. Because there can be multiple crystal phases present in the same particle as well as considering the contribution of the background, the APB-related local differences in intensity can be even more difficult to spot.

To determine the presence of the elusive APBs in real space, we employed atomically resolved STEM. Fig. 7a shows an atomically resolved HAADF STEM micrograph of a part of a nanoparticle exhibiting a faceted shape, a Pt-rich surface as evident from the higher intensity of surface atomic columns, and the presence of different crystal phases. From a series of atomic columns, alternating in intensity and mimicking the pattern, observed in simulated STEM images, it is possible to decipher an APB close to the particle surface. In Fig. 7b, a simulated image featuring a nanoparticle with an APB is shown to elucidate the alternating intensities in the case of a single-phase nanoparticle, while the comparison between the experimental and simulated result is depicted in Fig. 7c. On the experimentally obtained micrograph, a strict segmentation of the nanoparticle into definite single-phase regions is not possible due to the above-mentioned limitations concerning three-dimensionality and signal overlap from multiple phases. Nonetheless, local variations in intensity still enable us to confirm the presence of an anti-phase boundary. More STEM micrographs of that sample containing APBs can be found in Fig. S5, together with elemental maps in Fig. S6.

To determine their electrocatalytic affinity toward ORR, selected analogs were characterized using a TF-RDE setup. Weight fractions of Pt, measured with ICP-OES, did not differ significantly from sample to sample, as reported in Table S4. Similarly, all investigated samples contained nanoparticles with a Pt-rich surface, as evident from Fig. 7 and Fig. S7. The results for all four samples of a one-step synthesis are summarized in Table S5. The corresponding cyclic voltammograms, recorded during ORR polarization curve measurements and CO stripping measurements, as well as Tafel plots, are displayed in Fig. S8. These measurements illustrate the differences between ECSA values and catalytic activities from sample to sample. From the results, it was not possible to confirm a direct influence of the mere presence of APBs on the electrocatalytic properties, as the specific activity for the sample of the second set, containing APBs after annealing at 575 °C, was within the margin of error compared to the sample of the first set, i.e. the analog without clearly observable APBs but with a very similar weight fraction of

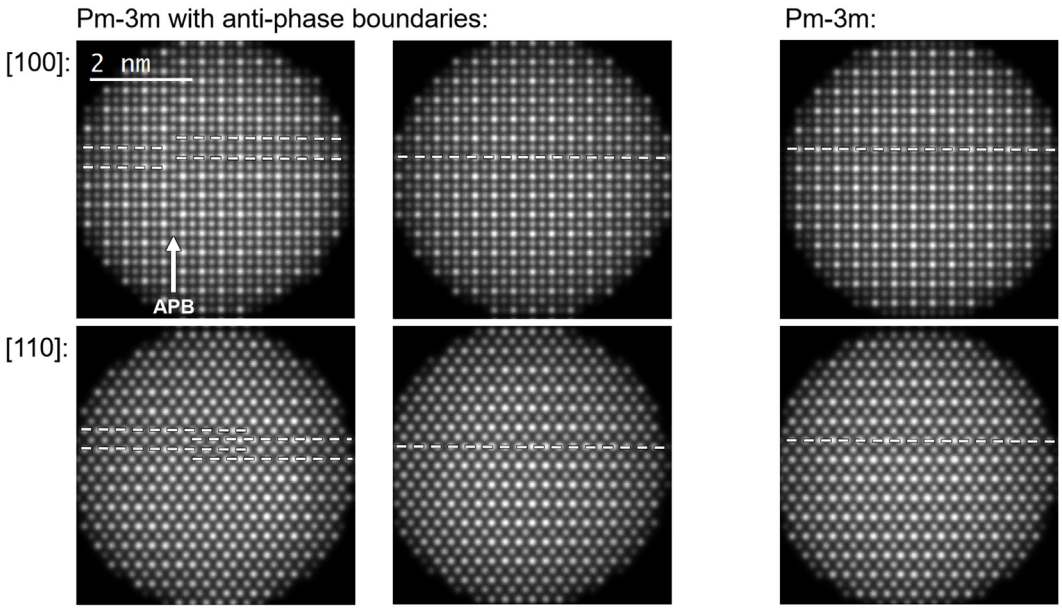

Fig. 6. QSTEM simulations of model nanoparticles. Models from a superstructure phase featuring an anti-phase boundary (left) and from a Pm-3m crystal phase (right) are imaged in [100] (top) and [110] (bottom) zone axes. Dashed lines and the arrow are used as a guide to the eye in tracking the positions of brighter atomic columns.

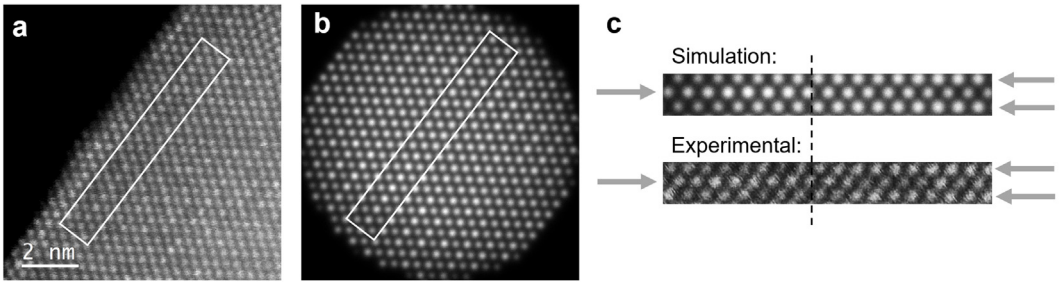

Fig. 7. STEM images of a Cu_3Pt nanoparticle containing an APB. **(a)** A STEM image of a part of a nanoparticle with a rectangle surrounding columns with alternating intensity, characteristic of APBs. **(b)** A simulated image of a nanoparticle containing an APB with a rectangle surrounding a set of columns with alternating intensity. **(c)** A comparison of column intensities around an APB. Arrows denote rows with higher-intensity columns on each side of the APB, which is denoted with a dashed line.

the disordered phase. The entirely disordered sample from the third set exhibited the lowest specific activity, while the sample from the fourth set, again containing APBs after subsequent annealing at 575 °C, exhibited a noticeably higher specific activity. A clear connection between specific activities and fractions of the disordered phase was revealed with a higher degree of disorder being associated with a lower specific activity, as plotted in Fig. 8. The observed trend is a clear indication that the presence of any ordered phase is very beneficial for Pt—Cu performance, which is in agreement with previous studies [11,16,51,63]. Meanwhile, the absence of APB impact on the specific activity can stem from size polydispersity, present in the investigated samples. APBs are more commonly present in larger nanoparticles, and the fraction of particle surface in contact with APBs is low, so APB-related sites contribute towards ECSA rather insignificantly.

All measured mass activities are notably higher than the 2020 mass activity target of 0.44 mA/g_{Pt} set by the US Department of Energy (DoE) [2,64]. They, however, remain only somewhat comparable to other catalysts based on nanoparticles from binary Pt-alloys, and quite modest compared to certain other reports of novel Pt-based ORR electrocatalysts, especially architectures such as hollow nanoframes, octahedra, and nanowires, which exhibit significantly higher mass activities than the presently reported

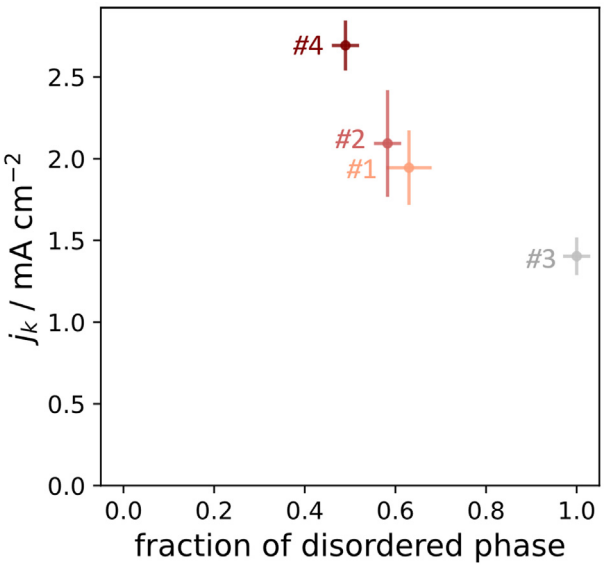

Fig. 8. Specific activity plotted against the weight fraction of the disordered Fm-3m phase for different Cu_3Pt/C electrocatalysts.

values [65]. Aside from supported Pt-based nanostructures, there are emerging options that lower the loading of metals even further and stand a chance to take over a part of the market [66]. Meanwhile, evaluating the electrochemical stability of the catalysts and comparing it against the US DoE targets is out of the scope of this study and requires further investigations. Similar supported platinum-copper nanoparticulate electrocatalysts were evaluated in the past and studies have confirmed a positive effect of alloy ordering on electrochemical stability [16]. However, those studies have not considered the presence of anti-phase boundaries. Therefore, further investigations are needed to properly establish the structure-stability relationship of the structures, presented in this work.

As there are indeed many different structural parameters at play when studying nanoparticulate electrocatalysts, broad investigations of bulk materials neglecting structural subtleties are not enough when attempting to explain their structure-property relationships. Focusing solely on, for instance, the degree of alloy ordering, or the presence of core-shell nanoparticulate structures, fails to consider the diversity of other parameters, like a wide range of defects in the crystal structure. Thus, taking existing studies on defect manifestation in bulk materials and transferring that knowledge to nanoparticulate electrocatalysts enables us a more detailed understanding of their crystal structure and a better chance of a more successful and tailored material synthesis in the future. A common theme in defect-oriented studies in electrocatalysis is an increased number of catalytically active sites as a consequence of the planar defects extending to the nanoparticle surface as well as an understanding of induced strains. However, studying anti-phase boundaries remains a severely unexplored topic in electrocatalysis. To better elucidate their link to the catalytically active sites and thus improve the defect-engineering approach, other local methods to probe an electrocatalytic surface should be employed, such as electrochemical scanning tunneling microscopy for the identification of different types or motifs of active sites. Lastly, to study such complex structures, a rather large amount of data needs to be gathered and analyzed, providing us with a great opportunity to introduce advanced data analysis to obtain objective and quantified information about our materials, thus eliminating human bias and being able to analyze more data than it would be reasonably possible to analyze manually [67].

4. Conclusions

In the present study, a Cu_3Pt/C nanoparticulate electrocatalyst containing anti-phase boundaries is reported. The APB-containing ordered alloy phase was investigated with XRD and STEM, supplemented by simulations to gain a comprehensive perspective on the structure under investigation. From the information about the bulk material, obtained with XRD, the weight fractions and unit cell parameters of all crystal phases were determined, namely Fm-3m, Pm-3m, and the superstructure phase, and the evolution of the APBs during a heating protocol was investigated with *in-situ* HT-XRD. The simulated diffraction patterns reveal that larger modulated pseudo-cubic cell sizes result in satellite peaks being closer together, while the number and prominence of satellite peaks are determined by APB placement with APBs near the middle of the cell causing fewer and less prominent satellite XRD peaks. HT-XRD measurement showed that the long-period superstructure appears at around 550 °C and disappears at around 590 °C and confirmed the thermodynamic stability of the structure within that temperature range. With higher temperatures, the satellite peaks appear closer together, indicating a growth in the size of the modulated unit cell. Trends about the local neighborhood of constituent atoms were confirmed with EXAFS analysis. Local information about the structure was obtained with electron microscopy, where electron diffraction and STEM imaging were used to provide proof of individual instances of APBs. The synthesized electrocatalysts were electrochemically evaluated using TF-RDE to elucidate the connection between the specific activity and degree of crystal disorder with more disordered samples having a lower specific activity. The presence of APBs, however, was not found to be correlated to the specific activity.

There remain certain challenges when engineering planar defects in nanoparticulate electrocatalysts and determining their impact on the catalytic properties. The presence of multiple structural anomalies makes the characterization and result interpretation more challenging even with advanced characterization techniques. Since the electrocatalysts' structure directly affects their properties, namely the electrochemical activity and stability, understanding those relationships is beneficial for an informed synthesis of novel materials. To deepen the understanding of the phenomena, observed in this work, future efforts will be focused on detailed electron microscopy including 3D and 4D imaging, and theoretical studies to elucidate the formation of defects and their impact on the catalysts' performance. Achieving synergy between information at the atomic scale and from the bulk material will help us reach this goal and enable better electrocatalysts for proton exchange membrane fuel cells and other applications.

CRediT author statement

A. R. Kamšek: Data curation, Formal analysis, Investigation, Methodology, Visualization, Writing - original draft, Writing - review & editing.

A. Meden: Formal analysis, Writing - review & editing.

I. Arčon: Formal analysis, Investigation, Writing - original draft, Writing - review & editing.

P. Jovanovič: Methodology, Writing - review & editing.

M. Šala: Investigation, Writing - review & editing.

F. Ruiz-Zepeda: Investigation, Writing - review & editing.

G. Dražić: Formal analysis, Investigation, Methodology, Supervision, Writing - review & editing.

M. Gaberšček: Writing - review & editing.

M. Bele: Conceptualization, Investigation, Methodology, Supervision, Writing - original draft, Writing - review & editing.

N. Hodnik: Funding acquisition, Supervision, Writing - original draft, Writing - review & editing.

Declaration of competing interest

The authors declare that they have no known competing financial interests or personal relationships that could have appeared to influence the work reported in this paper.

Data availability

Data will be made available on request.

Acknowledgments

The authors thank Edi Kranjc for XRD measurements. The authors would like to acknowledge the Slovenian research agency (ARRS) programs P2-0393, I0-0003, P1-0112, P1-0175, P1-0034, P2-0421; the projects NC-0007, NC-0016, N2-0155, N2-0257, J2-3041; European Research Council (ERC) Starting Grant 123STABLE (Grant agreement ID: 852208) and NATO Science for Peace and Security Program under grant G5729. Access to synchrotron radiation facilities of ELETTRA (project 20215267, beamline XAFS) and assistance during the experiment, as well as expert advice on beamline

operation by Giuliana Aquilanti, Gangadhar Das, and Ricardo Grisonich from XAFS beamline of ELETTRA, are acknowledged. A.R.K. would like to acknowledge the support of the Milan Lenarčič Foundation and the Janko Jamnik Doctoral Scholarship.

Appendix A. Supplementary data

Supplementary data to this article can be found online at https://doi.org/10.1016/j.mtnano.2023.100377.

References

[1] D. Banham, S. Ye, Current status and future development of catalyst materials and catalyst layers for proton exchange membrane fuel cells: an industrial perspective, ACS Energy Lett. 2 (2017) 629–638, https://doi.org/10.1021/acsenergylett.6b00644.
[2] H.Y. Kim, J.Y. Kim, S.H. Joo, Pt-based intermetallic nanocatalysts for promoting the oxygen reduction reaction, Bull. Korean Chem. Soc. 42 (2021) 724–736, https://doi.org/10.1002/bkcs.12274.
[3] A.S. Bandarenka, M.T.M. Koper, Structural and electronic effects in heterogeneous electrocatalysis: toward a rational design of electrocatalysts, J. Catal. 308 (2013) 11–24, https://doi.org/10.1016/j.jcat.2013.05.006.
[4] M. Luo, S. Guo, Strain-controlled electrocatalysis on multimetallic nanomaterials, Nat. Rev. Mater. 2 (2017) 1–14, https://doi.org/10.1038/natrevmats.2017.59.
[5] B. Garlyyev, J. Fichtner, O. Piqué, O. Schneider, A.S. Bandarenka, F. Calle-Vallejo, Revealing the nature of active sites in electrocatalysis, Chem. Sci. 10 (2019) 8060–8075, https://doi.org/10.1039/c9sc02654a.
[6] S. Kim, J. Kwag, C. Machello, S. Kang, J. Heo, C.F. Reboul, D. Kang, S. Kang, S. Shim, S. Park, B.H. Kim, T. Hyeon, P. Ercius, H. Elmlund, J. Park, Correlating 3D surface atomic structure and catalytic activities of Pt nanocrystals, Nano Lett. 21 (2021) 1175–1183, https://doi.org/10.1021/acs.nanolett.0c04873.
[7] L.J. Moriau, A. Hrnjić, A. Pavlišič, A.R. Kamšek, U. Petek, F. Ruiz-Zepeda, M. Šala, L. Pavko, V.S. Šelih, M. Bele, P. Jovanovič, M. Gatalo, N. Hodnik, Resolving the nanoparticles' structure-property relationships at the atomic level: a study of Pt-based electrocatalysts, iScience 24 (2021) 102102, https://doi.org/10.1016/j.isci.2021.102102.
[8] K. Kodama, T. Nagai, A. Kuwaki, R. Jinnouchi, Y. Morimoto, Challenges in applying highly active Pt-based nanostructured catalysts for oxygen reduction reactions to fuel cell vehicles, Nat. Nanotechnol. 16 (2021) 140–147, https://doi.org/10.1038/s41565-020-00824-w.
[9] S. Zaman, L. Huang, A.I. Douka, H. Yang, B. You, B.Y. Xia, Oxygen reduction electrocatalysts toward practical fuel cells: progress and perspectives, Angew. Chem. Int. Ed. 60 (2021) 17832–17852, https://doi.org/10.1002/anie.202016977.
[10] K. Ehelebe, D. Escalera-López, S. Cherevko, Limitations of aqueous model systems in the stability assessment of electrocatalysts for oxygen reactions in fuel cell and electrolyzers, Curr. Opin. Electrochem. 29 (2021) 100832, https://doi.org/10.1016/j.coelec.2021.100832.
[11] M. Gatalo, F. Ruiz-Zepeda, N. Hodnik, G. Dražić, M. Bele, M. Gaberšček, Insights into thermal annealing of highly-active $PtCu_3$/C Oxygen Reduction Reaction electrocatalyst: an in-situ heating transmission electron microscopy study, Nano Energy 63 (2019) 103892, https://doi.org/10.1016/j.nanoen.2019.103892.
[12] M. Oezaslan, F. Hasché, P. Strasser, In situ observation of bimetallic alloy nanoparticle formation and growth using high-temperature XRD, Chem. Mater. 23 (2011) 2159–2165, https://doi.org/10.1021/cm103661q.
[13] X. Chen, S. Zhang, C. Li, Z. Liu, X. Sun, S. Cheng, D.N. Zakharov, S. Hwang, Y. Zhu, J. Fang, G. Wang, G. Zhou, Composition-dependent ordering transformations in Pt-Fe nanoalloys, Proc. Natl. Acad. Sci. USA 119 (2022) 1–10, https://doi.org/10.1073/pnas.2117899119.
[14] W.J. Zeng, C. Wang, Q.Q. Yan, P. Yin, L. Tong, H.W. Liang, Phase diagrams guide synthesis of highly ordered intermetallic electrocatalysts: separating alloying and ordering stages, Nat. Commun. 13 (2022), https://doi.org/10.1038/s41467-022-35457-1.
[15] Y. Xiong, Y. Yang, H. Joress, E. Padgett, U. Gupta, V. Yarlagadda, D.N. Agyeman-Budu, X. Huang, T.E. Moylan, R. Zeng, A. Kongkanand, F.A. Escobedo, J.D. Brock, F.J. DiSalvo, D.A. Muller, H.D. Abruña, Revealing the atomic ordering of binary intermetallics using in situ heating techniques at multilength scales, Proc. Natl. Acad. Sci. USA 116 (2019) 1974–1983, https://doi.org/10.1073/pnas.1815643116.
[16] A. Pavlišič, P. Jovanovič, V.S. Šelih, M. Šala, M. Bele, G. Dražić, I. Arčon, S. Hočevar, A. Kokalj, N. Hodnik, M. Gaberšček, Atomically resolved dealloying of structurally ordered Pt nanoalloy as an oxygen reduction reaction electrocatalyst, ACS Catal. 6 (2016) 5530–5534, https://doi.org/10.1021/acscatal.6b00557.
[17] C.-L. Yang, L.-N. Wang, P. Yin, J. Liu, M.-X. Chen, Q.-Q. Yan, Z.-S. Wang, S.-L. Xu, S.-Q. Chu, C. Cui, H. Ju, J. Zhu, Y. Lin, J. Shui, H.-W. Liang, Sulfur-anchoring synthesis of platinum intermetallic nanoparticle catalysts for fuel cells, Science 374 (2021) 459–464, https://doi.org/10.1126/science.abj9980.
[18] S. Ogawa, H. Iwasaki, A. Terada, Study of the long-period ordered alloy Cu_3Pt, J. Phys. Soc. Japan 34 (1973) 384–390, https://doi.org/10.1143/JPSJ.34.384.
[19] S. Kubo, K. Adachi, Origin of the formation of one- and two-dimensional long period superlattices in Cu-Pd and Cu-Pt systems, J. Phys. Soc. Japan 35 (1973) 776–783, https://doi.org/10.1143/JPSJ.35.776.
[20] N. Kuwano, R. Nakayama, K. Oki, Transformation processes from short range Order to $L1_2$ and $L1_{2\text{-}S}$ ordered states in a Cu-25.7 at% Pt alloy, Trans Jpn Inst Met 28 (1987) 7, https://doi.org/10.2320/matertrans1960.28.1.
[21] N. Kuwano, N. Chiwata, K. Oki, In situ TEM observation of long range ordering via short range order in Cu_3Pt, Bull. Mater. Sci. 22 (1999) 697–700, https://doi.org/10.1007/BF02749988.
[22] E.W. Collings, R.D. Smith, J.C. Ho, Magnetic investigations of order-disorder transitions in copper-platinum (12.5 - 27.5 at. %) alloys, J. Less Common. Met. 46 (1976) 189–195, https://doi.org/10.1016/0022-5088(76)90209-5.
[23] S. Takeda, J. Kulik, D. De Fontaine, One-dimensional long-period superstructures in Cu_3Pd observed by high-resolution electron microscopy, J. Phys. F Met. Phys. 18 (1988) 1387–1404, https://doi.org/10.1088/0305-4608/18/7/009.
[24] O.I. Velikokhatnyi, S.V. Eremeev, I.I. Naumov, A.I. Potekaev, Electronic structure and character of long-period superstructures in precious-metal alloys, Comput. Mater. Sci. 19 (2000) 275–284, https://doi.org/10.1016/S0927-0256(00)00164-6.
[25] C. Rentenberger, H.P. Karnthaler, Extensive disordering in long-range-ordered Cu_3Au induced by severe plastic deformation studied by transmission electron microscopy, Acta Mater. 56 (2008) 2526–2530, https://doi.org/10.1016/j.actamat.2008.01.035.
[26] P. Scardi, M. Leoni, Diffraction whole-pattern modelling study of anti-phase domains in Cu_3Au, Acta Mater. 53 (2005) 5229–5239, https://doi.org/10.1016/j.actamat.2005.08.002.
[27] A. Lak, S. Disch, P. Bender, Embracing defects and disorder in magnetic nanoparticles, Adv. Sci. 8 (2021), https://doi.org/10.1002/advs.202002682.
[28] K.P. McKenna, F. Hofer, D. Gilks, V.K. Lazarov, C. Chen, Z. Wang, Y. Ikuhara, Atomic-scale structure and properties of highly stable antiphase boundary defects in Fe_3O_4, Nat. Commun. 5 (2014), https://doi.org/10.1038/ncomms6740.
[29] C. Frommen, H. Rösner, Observation of long-period superstructures in chemically synthesised CoPt nanoparticles, Mater. Lett. 58 (2004) 123–127, https://doi.org/10.1016/S0167-577X(03)00428-2.
[30] J.E. Wittig, J. Bentley, L.F. Allard, J. Bentley, In situ investigation of ordering phase transformations in FePt magnetic nanoparticles, Ultramicroscopy 176 (2017) 218–232, https://doi.org/10.1016/j.ultramic.2016.11.025.
[31] R. Chattot, P. Bordet, I. Martens, J. Drnec, L. Dubau, F. Maillard, Building practical descriptors for defect engineering of electrocatalytic materials, ACS Catal. 10 (2020) 9046–9056, https://doi.org/10.1021/acscatal.0c02144.
[32] J. Lee, C. Jeong, T. Lee, S. Ryu, Y. Yang, Direct observation of three-dimensional atomic structure of twinned metallic nanoparticles and their catalytic properties, Nano Lett. 22 (2022) 665–672, https://doi.org/10.1021/acs.nanolett.1c03773.
[33] X. Wang, L. Figueroa-Cosme, X. Yang, M. Luo, J. Liu, Z. Xie, Y. Xia, Pt-based icosahedral nanocages: using a combination of {111} facets, twin defects, and ultrathin walls to greatly enhance their activity toward oxygen reduction, Nano Lett. 16 (2016) 1467–1471, https://doi.org/10.1021/acs.nanolett.5b05140.
[34] X. Sun, K. Jiang, N. Zhang, S. Guo, X. Huang, Crystalline control of {111} bounded Pt_3Cu nanocrystals: multiply-twinned Pt_3Cu icosahedra with enhanced electrocatalytic properties, ACS Nano 9 (2015) 7634–7640, https://doi.org/10.1021/acsnano.5b02986.
[35] D. Fang, L. Wan, Q. Jiang, H. Zhang, X. Tang, X. Qin, Z. Shao, Z. Wei, Wavy PtCu alloy nanowire networks with abundant surface defects enhanced oxygen reduction reaction, Nano Res. 12 (2019) 2766–2773, https://doi.org/10.1007/s12274-019-2511-8.
[36] Z. Zhang, Z. Luo, B. Chen, C. Wei, J. Zhao, J. Chen, X. Zhang, Z. Lai, Z. Fan, C. Tan, M. Zhao, Q. Lu, B. Li, Y. Zong, C. Yan, G. Wang, Z.J. Xu, H. Zhang, One-pot synthesis of highly anisotropic five-fold-twinned PtCu nanoframes used as a bifunctional electrocatalyst for oxygen reduction and methanol oxidation, Adv. Mater. 28 (2016) 8712–8717, https://doi.org/10.1002/adma.201603075.
[37] X.J. Liu, X. Yin, Y.D. Sun, F.J. Yu, X.W. Gao, L.J. Fu, Y.P. Wu, Y.H. Chen, Interlaced Pd-Ag nanowires rich in grain boundary defects for boosting oxygen reduction electrocatalysis, Nanoscale 12 (2020) 5368–5373, https://doi.org/10.1039/d0nr00046a.
[38] Y. Qin, W. Zhang, K. Guo, X. Liu, J. Liu, X. Liang, X. Wang, D. Gao, L.Y. Gan, Y. Zhu, Z. Zhang, W. Hu, Fine-tuning intrinsic strain in penta-twinned Pt–Cu–Mn nanoframes boosts oxygen reduction catalysis, Adv. Funct. Mater. 30 (2020), https://doi.org/10.1002/adfm.201910107.
[39] M.K. Kabiraz, S. Il Choi, Revisit to grain boundary effect in Pt nanocrystals toward the oxygen electroreduction reaction, ChemCatChem (2023), https://doi.org/10.1002/cctc.202300454.
[40] M.K. Kabiraz, B. Ruqia, J. Kim, H. Kim, H.J. Kim, Y. Hong, M.J. Kim, Y.K. Kim, C. Kim, W.J. Lee, W. Lee, G.H. Hwang, H.C. Ri, H. Baik, H.S. Oh, Y.W. Lee, L. Gao, H. Huang, S.M. Paek, Y.J. Jo, C.H. Choi, S.W. Han, S. Il Choi, Understanding the grain boundary behavior of bimetallic platinum-cobalt alloy nanowires toward oxygen electro-reduction, ACS Catal. 12 (2022) 3516–3523, https://doi.org/10.1021/acscatal.1c05766.
[41] X. Geng, S. Li, J. Heo, Y. Peng, W. Hu, Y. Liu, J. Huang, Y. Ren, D. Li, L. Zhang, L. Luo, Grain-boundary-rich noble metal nanoparticle assemblies: synthesis,

characterization, and reactivity, Adv. Funct. Mater. 32 (2022), https://doi.org/10.1002/adfm.202204169.
[42] K. Liu, W. Wang, P. Guo, J. Ye, Y. Wang, P. Li, Z. Lyu, Y. Geng, M. Liu, S. Xie, Replicating the defect structures on ultrathin Rh nanowires with Pt to achieve superior electrocatalytic activity toward ethanol oxidation, Adv. Funct. Mater. 29 (2019), https://doi.org/10.1002/adfm.201806300.
[43] H. You, F. Gao, C. Wang, J. Li, K. Zhang, Y. Zhang, Y. Du, Rich grain boundaries endow networked PdSn nanowires with superior catalytic properties for alcohol oxidation, Nanoscale 13 (2021) 17939–17944, https://doi.org/10.1039/d1nr04993c.
[44] X. Feng, K. Jiang, S. Fan, M.W. Kanan, Grain-boundary-dependent CO_2 electroreduction activity, J. Am. Chem. Soc. 137 (2015) 4606–4609, https://doi.org/10.1021/ja5130513.
[45] X. Feng, K. Jiang, S. Fan, M.W. Kanan, A direct grain-boundary-activity correlation for CO electroreduction on Cu nanoparticles, ACS Cent. Sci. 2 (2016) 169–174, https://doi.org/10.1021/acscentsci.6b00022.
[46] X. Zhang, X. Li, Z. Pan, Y. Lai, Y. Lu, Y. Wang, S. Song, Boosting hydrogen evolution electrocatalysis through defect engineering: a strategy of heat and cool shock, Chem. Eng. J. 426 (2021), https://doi.org/10.1016/j.cej.2021.131524.
[47] Z. Li, J.Y. Fu, Y. Feng, C.K. Dong, H. Liu, X.W. Du, A silver catalyst activated by stacking faults for the hydrogen evolution reaction, Nat Catal 2 (2019) 1107–1114, https://doi.org/10.1038/s41929-019-0365-9.
[48] H. Huang, Y. Wei, B. Shen, Y. Zhang, H. He, Q. Jiang, L. Yang, A.K. Nanjundan, J. Na, X. Xu, J. Zhu, Y. Yamauchi, Synthesis of multiple-twinned Pd nanoparticles anchored on graphitic carbon nanosheets for use as highly-active multifunctional electrocatalyst in formic acid and methanol oxidation reactions, Adv. Mater. Interfac. 7 (2020), https://doi.org/10.1002/admi.202000142.
[49] W. Huang, A.C. Johnston-Peck, T. Wolter, W.-C.D. Yang, L. Xu, J. Oh, B.A. Reeves, C. Zhou, M.E. Holtz, A.A. Herzing, A.M. Lindenberg, M. Mavrikakis, M. Cargnello, Steam-created grain boundaries for methane C-H activation in palladium catalysts, Science 373 (2021) 1518–1523, https://doi.org/10.1126/science.abj5291.
[50] Y.T. Pan, Y. Yan, Y.T. Shao, J.M. Zuo, H. Yang, Ag-Pt compositional intermetallics made from alloy nanoparticles, Nano Lett. 16 (2016) 6599–6603, https://doi.org/10.1021/acs.nanolett.6b03302.
[51] M. Bele, P. Jovanovič, A. Pavlišič, B. Jozinović, M. Zorko, A. Rečnik, E. Chernyshova, S. Hočevar, N. Hodnik, M. Gaberšček, A highly active $PtCu_3$ intermetallic core–shell, multilayered Pt-skin, carbon embedded electrocatalyst produced by a scale-up sol–gel synthesis, Chem. Commun. 50 (2014) 13124–13126, https://doi.org/10.1039/c4cc05637j.
[52] Marjan Bele, Miran Gaberscek, Gregor Kapun, Nejc Hodnik, Stanko Hocevar, Electrocatalytic Composite(s), Associated Composition(s), and Associated Process(es), US20130045866A1, 2012.
[53] N. Hodnik, M. Zorko, M. Bele, S. Hočevar, M. Gaberšček, Identical location scanning electron microscopy: a case study of electrochemical degradation of PtNi nanoparticles using a new nondestructive method, J. Phys. Chem. C 116 (2012) 21326–21333, https://doi.org/10.1021/jp303831c.
[54] F. Xiao, X. Qin, M. Xu, S. Zhu, L.L. Zhang, Y. Hong, S. Il Choi, Q. Chang, Y. Xu, X. Pan, M. Shao, Impact of heat treatment on the electrochemical properties of carbon-supported octahedral Pt-Ni nanoparticles, ACS Catal. 9 (2019) 11189–11198, https://doi.org/10.1021/acscatal.9b03206.
[55] B.H. Toby, R.B. von Dreele, GSAS-II: the genesis of a modern open-source all purpose crystallography software package, J. Appl. Crystallogr. 46 (2013) 544–549, https://doi.org/10.1107/S0021889813003531.
[56] A.A. Coelho, TOPAS and TOPAS-Academic: an optimization program integrating computer algebra and crystallographic objects written in C++, J Appl Crystallogr 51 (2018) 210–218, https://doi.org/10.1107/S1600576718000183.
[57] M.M.J. Treacy, J.M. Newsam, M.W. Deem, A general recursion method for calculating diffracted intensities from crystals containing planar faults, Proc R Soc London Ser A 433 (1991) 499–520, https://doi.org/10.1098/rspa.1991.0062.
[58] C. Koch, Determination of Core Structure Periodicity and Point Defect Density along Dislocations, Arizona State University, 2002.
[59] D. van der Vliet, D.S. Strmcnik, C. Wang, V.R. Stamenkovic, N.M. Markovic, M.T.M. Koper, On the importance of correcting for the uncompensated Ohmic resistance in model experiments of the Oxygen Reduction Reaction, J. Electroanal. Chem. 647 (2010) 29–34, https://doi.org/10.1016/j.jelechem.2010.05.016.
[60] K.J.J. Mayrhofer, D. Strmcnik, B.B. Blizanac, V. Stamenkovic, M. Arenz, N.M. Markovic, Measurement of oxygen reduction activities via the rotating disc electrode method: from Pt model surfaces to carbon-supported high surface area catalysts, Electrochim. Acta 53 (2008) 3181–3188, https://doi.org/10.1016/j.electacta.2007.11.057.
[61] T. Abe, B. Sundman, H. Onodera, Thermodynamic assessment of the Cu-Pt system, J. Phase Equilibria Diffus. 27 (2006) 5–13, https://doi.org/10.1361/105497196X92736.
[62] N. Kuwano, A. Matsumoto, K. Kajiwara, K. Oki, Annihilation process of periodic antiphase boundaries in Cu_3Pt studied with time dependent Ginzburg Landau model, Mater. Trans. 34 (1993) 1163–1168, https://doi.org/10.2320/matertrans1989.34.1163.
[63] E. Antolini, Alloy vs. intermetallic compounds: effect of the ordering on the electrocatalytic activity for oxygen reduction and the stability of low temperature fuel cell catalysts, Appl. Catal., B 217 (2017) 201–213, https://doi.org/10.1016/j.apcatb.2017.05.081.
[64] Hydrogen and Fuel Cell Technologies Office, Hydrogen and Fuel Cell Technologies Office Multi-Year Research, Development, and Demonstration Plan, 2014. https://www.energy.gov/eere/fuelcells/articles/hydrogen-and-fuel-cell-technologies-office-multi-year-research-development. (Accessed 7 March 2023).
[65] L. Huang, S. Zaman, X. Tian, Z. Wang, W. Fang, B.Y. Xia, Advanced platinum-based oxygen reduction electrocatalysts for fuel cells, Acc. Chem. Res. 54 (2021) 311–322, https://doi.org/10.1021/acs.accounts.0c00488.
[66] J.P. Zhong, C. Hou, M.L. Sun, Z.Y. Yang, D.H. Chen, Y.J. Fan, W. Chen, H.G. Liao, S.G. Sun, A superior electrocatalyst toward the oxygen reduction reaction obtained by atomically dispersing copper on N, F co-doped graphene through atomic interface engineering, J Mater Chem A Mater 10 (2022) 13876–13883, https://doi.org/10.1039/d2ta01990f.
[67] J.M. Rickman, T. Lookman, S.V. Kalinin, Materials informatics: from the atomic-level to the continuum, Acta Mater. 168 (2019) 473–510, https://doi.org/10.1016/j.actamat.2019.01.051.